UNIVERSITÄT AUGSBURG
Universitätsbibliothek

OPEN ACCESS
OPUS AUGSBURG

First measurements of an imaging heavy ion beam probe at the ASDEX Upgrade tokamak

J. Galdon-Quiroga, Gregor Birkenmeier, P. Oyola, H. Lindl, A. Rodriguez-Gonzalez, G. Anda, M. Garcia-Munoz, A. Herrmann, J. Kalis, K. Kaunert, T. Lunt, D. Refy, V. Rohde, J. Rueda-Rueda, M. Sochor, B. Tal, M. Teschke, M. Videla, E. Viezzer, S. Zoletnik

Angaben zur Veröffentlichung / Publication details:

Galdon-Quiroga, J., Gregor Birkenmeier, P. Oyola, H. Lindl, A. Rodriguez-Gonzalez, G. Anda, M. Garcia-Munoz, et al. 2024. "First measurements of an imaging heavy ion beam probe at the ASDEX Upgrade tokamak." *Review of Scientific Instruments* 95: 013504. https://doi.org/10.1063/5.0175720.

Nutzungsbedingungen / Terms of use: **CC BY 4.0**

Dieses Dokument wird unter folgenden Bedingungen zur Verfügung gestellt: / This document is made available under these conditions:
CC-BY 4.0: Creative Commons: Namensnennung
Weitere Informationen finden Sie unter: / For more information see:
https://creativecommons.org/licenses/by/4.0/deed.de

Review of Scientific Instruments

RESEARCH ARTICLE | JANUARY 11 2024

First measurements of an imaging heavy ion beam probe at the ASDEX Upgrade tokamak

J. Galdon-Quiroga ; G. Birkenmeier ; P. Oyola ; H. Lindl ; A. Rodriguez-Gonzalez ; G. Anda ; M. Garcia-Munoz ; A. Herrmann ; J. Kalis ; K. Kaunert; T. Lunt ; D. Refy ; V. Rohde ; J. Rueda-Rueda ; M. Sochor; B. Tal; M. Teschke; M. Videla ; E. Viezzer; S. Zoletnik ; ASDEX Upgrade Team

Check for updates

Rev. Sci. Instrum. 95, 013504 (2024)
https://doi.org/10.1063/5.0175720

View Online
Export Citation

Articles You May Be Interested In

Validation of the synthetic model for the imaging heavy ion beam probe at the ASDEX Upgrade tokamak (invited)

Rev. Sci. Instrum. (August 2024)

Implementation of synthetic fast-ion loss detector and imaging heavy ion beam probe diagnostics in the 3D hybrid kinetic-MHD code MEGA

Rev. Sci. Instrum. (April 2021)

Applicability of alkali beam emission spectroscopy on NSTX-U

Rev. Sci. Instrum. (September 2024)

03 November 2026 15:33:44



AIP Publishing

Review of Scientific Instruments ARTICLE pubs.aip.org/aip/rsi

First measurements of an imaging heavy ion beam probe at the ASDEX Upgrade tokamak

Cite as: Rev. Sci. Instrum. 95, 013504 (2024); doi: 10.1063/5.0175720
Submitted: 8 September 2023 • Accepted: 18 December 2023 •
Published Online: 11 January 2024

View Online Export Citation CrossMark

J. Galdon-Quiroga,[1,a)] G. Birkenmeier,[2,3] P. Oyola,[1] H. Lindl,[2,3] A. Rodriguez-Gonzalez,[1] G. Anda,[4] M. Garcia-Munoz,[1] A. Herrmann,[2] J. Kalis,[2,3] K. Kaunert,[2] T. Lunt,[2] D. Refy,[4] V. Rohde,[2] J. Rueda-Rueda,[1] M. Sochor,[2] B. Tal,[2] M. Teschke,[2] M. Videla,[1] E. Viezzer,[1] S. Zoletnik,[4] and ASDEX Upgrade Team[2,b)]

AFFILIATIONS

[1] Department of Atomic, Molecular and Nuclear Physics, University of Seville, Seville, Spain
[2] Max Planck Institute for Plasma Physics, Garching, Germany
[3] TUM School of Natural Sciences, Physics Department, Technical University of Munich, 85748 Garching, Germany
[4] Centre for Energy Research, Budapest, Hungary

[a)] **Author to whom correspondence should be addressed:** jgaldon@us.es
[b)] See author list of U. Stroth *et al.*, Nucl. Fusion **62**, 042006 (2022).

03 November 2026 15:33:44

ABSTRACT

The imaging heavy ion beam probe (i-HIBP) diagnostic has been successfully commissioned at ASDEX Upgrade. The i-HIBP injects a primary neutral beam into the plasma, where it is ionized, leading to a fan of secondary (charged) beams. These are deflected by the magnetic field of the tokamak and collected by a scintillator detector, generating a strike-line light pattern that encodes information on the density, electrostatic potential, and magnetic field of the plasma edge. The first measurements have been made, demonstrating the proof-of-principle of this diagnostic technique. A primary beam of $^{85/87}$Rb has been used with energies ranging between 60 and 72 keV and extracted currents up to 1.5 mA. The first signals have been obtained in experiments covering a wide range of parameter spaces, with plasma currents (I_p) between 0.2 and 0.8 MA and on-axis toroidal magnetic field (B_t) between 1.9 and 2.7 T. Low densities appear to be critical for the performance of the diagnostic, as signals are typically observed only when the line integrated density is below 2.0–3.0 × 10^{19} m^{-2} in the central interferometer chord, depending on the plasma shape. The strike line moves as expected when I_p is ramped, indicating that current measurements are possible. Additionally, clear dynamics in the intensity of the strike line are often observed, which might be linked to changes in the edge profile structure. However, the signal-to-background ratio of the signals is hampered by stray light, and the image guide degradation is due to neutron irradiation. Finally, simulations have been carried out to investigate the sensitivity of the expected signals to plasma density and temperature. The results are in qualitative agreement with the experimental observations, suggesting that the diagnostic is almost insensitive to fluctuations in the temperature profile, while the signal level is highly determined by the density profile due to the beam attenuation.

© 2024 Author(s). All article content, except where otherwise noted, is licensed under a Creative Commons Attribution (CC BY) license (http://creativecommons.org/licenses/by/4.0/). https://doi.org/10.1063/5.0175720

I. INTRODUCTION

In magnetically confined fusion plasmas, the experimental characterization of magnetohydrodynamic (MHD) instabilities and turbulence is crucial for the understanding of particle and energy transport mechanisms. To this end, measurements of various quantities such as plasma density, temperature, electrostatic potential, and magnetic field (among others) with good spatial and temporal resolution are desired. For many years, heavy ion beam probes (HIBPs) have served this purpose by providing measurements of plasma density, potential, and poloidal magnetic field fluctuations across the whole plasma volume of tokamaks and stellarator devices.[1–3] Indeed, HIBPs have contributed to a variety of studies, including different phenomena such as zonal flows,[4,5] zonal magnetic field generation,[6] L-H transition,[7,8] or energetic particle driven instabilities,[9–11] among others. Standard HIBPs typically

rely on the use of a high-energy charged heavy ion primary beam that is launched into the plasma. The primary beam then suffers additional ionizations, thus changing its charge state and, consequently, its trajectory. The secondary beam is collected by a detector, typically an electrostatic energy analyzer, which allows us to infer plasma properties at a localized plasma region defined by the ionization volume in the plasma. The probing volume can, therefore, be tuned by adjusting the beam trajectory through the primary beam energy. Techniques have been developed that can provide a sequential measurement at different plasma volumes[12–14] as well as density fluctuations[15] and density profile reconstruction measurements.[16,17]

Motivated by the need for such a system for the ASDEX Upgrade tokamak, a new diagnostic concept based on standard HIBP was proposed. The imaging heavy ion beam probe (i-HIBP) features two main differences from the standard HIBP. First, the use of a neutral primary beam allows us to use lower injection energies, thus reducing the size and complexity of the system. Second, a scintillator detector is used as an active component, which potentially allows for simultaneous measurement of multiple plasma volumes with improved spatial resolution. A detailed description of the concept can be found in Refs. 18–20, so only a brief overview of the working principle is given here. A neutral primary beam is injected into the plasma. As the primary beam penetrates, it gets ionized, creating a fan of secondary singly ionized beams whose trajectories are deflected by the electromagnetic fields of the device. This fan of secondary beams is collected by a scintillator screen, which is placed in the first wall of the device, creating a characteristic light pattern dubbed the strike line. Information about the density, electrostatic potential, and magnetic field can be inferred from the strike line intensity and displacements. The system shares some similarities with the atomic beam probe concept[21–26] and the heavy neutral beam probe concept[27–30] but differs in the use of a scintillator detector instead of a multi-channel Faraday cup detector.[25,31,32]

In this work, we report the first experimental signals obtained with the i-HIBP diagnostic installed at the ASDEX Upgrade tokamak. In Sec. II, the experimental setup is reviewed. In Sec. III, the results of simulations to investigate the sensitivity of the diagnostic to density and temperature variations are presented. In Sec. IV, the commissioning of the system and the experiments leading to the first signals are described, along with a discussion on the performance, limitations, and possible upgrades of the diagnostic. Finally, in Sec. V, a summary is provided.

II. EXPERIMENTAL SETUP

The diagnostic structure can be divided into two main parts: the beam injector and the detection system. In Subsections II A and II B, these two are described.

A. Beam injector

The beam injector is based on the design of alkali beam injectors,[33] which are widely used in the field for beam emission

03 November 2026 15:33:44

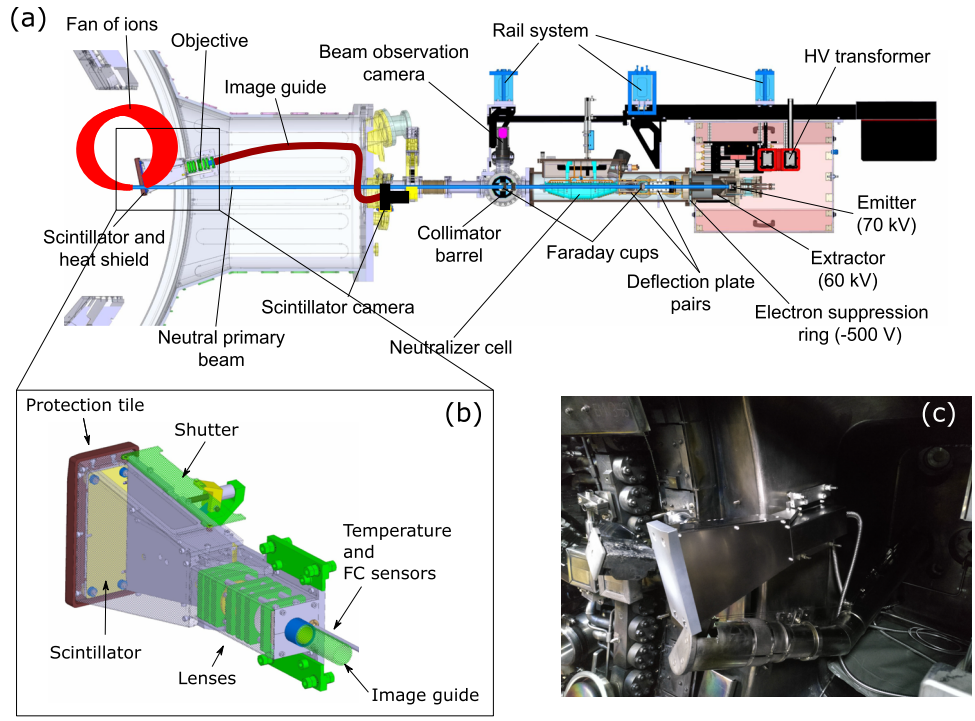

FIG. 1. (a) Overview of the iHIBP injector setup at ASDEX Upgrade. Reproduced with permission from J. Instrum. **14**, C10030 (2019).[19] Copyright 2019 IOP Publishing, Ltd. and Sissa Medialab. (b) Detailed CAD of the detector head. (c) Picture of the installed setup at the ASDEX Upgrade tokamak, in sector 13.

© Author(s) 2024

spectroscopy diagnostics. A schematic view of the AUG system is shown in Fig. 1, which is installed at the midplane port of sector 13. The first parts of the system are the ion source and the high voltage components. The system is designed to operate at voltages up to 80 kV; therefore, for safety reasons, the whole high-voltage (HV) system is embedded in a cage. The emitter is set to HV according to the aimed beam energy (e.g., 70 kV). The extractor is set to a lower voltage, between 1 and 10 kV less, which creates the necessary electric field to extract the ions from the source. The ions are further accelerated toward the beam-line by the voltage difference between the extractor electrode and the ground electrode at the beginning of the flight tube. An electron suppression ring biased to −500 V prevents electrons from flying back to the source, which could potentially damage it. Two pairs of deflection plates allow us to adjust the beam direction horizontally and vertically. This is followed by the neutralizer cell. It contains between 5 and 10 g of Na, which is heated up to 260–280 °C. The side cones are kept at 100–130 °C, leading to the condensation of the Na vapor and thus minimizing the flow of Na vapor out of the neutralizer cell. The diagnostic chamber follows after the neutralizer cell. It contains two cameras for beam monitoring and a set of mechanical collimators to adjust the beam size. The beam is then injected into the tokamak vacuum chamber. In order to monitor the beam size and shape along the flight tube, two Faraday cups (FC) can be inserted into the beamline: FC1, right after the beam deflection plates, and FC2, in the diagnostic chamber. For a detailed description of all the components, the reader is referred to Refs. 19 and 33.

In AUG, two different sources have been used: Cs and Rb during the 2020–2021 and 2021–2022 experimental campaigns, respectively. In both cases, extracted currents of up to 1.5 mA were obtained. This is illustrated in Fig. 2, where the extracted beam current is represented against the extraction voltage for Cs and Rb sources at different temperatures. It can be observed that at low extraction voltages, the experimental curve fits well with the Child–Langmuir curve, indicating that the extracted current is limited by space-charge effects. At higher extraction voltages, the extracted current stays below the Child–Langmuir curve, indicating that the extraction of current is limited by the temperature of the source. This can be seen by comparing cases at different source heating currents: for higher source temperatures, the extracted current saturates at higher levels. In both cases, a neutralizing efficiency of up to 80% can be obtained. The neutralization efficiency ϵ_n is measured as described in Ref. 33,

$$\epsilon_n = \frac{I_n}{I_i} = \frac{I_2^n - (1+\alpha) I_1^n}{\alpha \cdot I_i}, \tag{1}$$

where I_i is the extracted ion current, I_n is the neutral beam equivalent current, and I_1^n and I_2^n are the currents measured at FC2 with the neutralizer on with a negative and positive 500 V bias at the FC, respectively. Here, α is the number of secondary electrons emitted per incident ion.

The beam size and shape are determined by the extraction voltage as well. The system is experimentally optimized to improve the focusing of the beam at FC2. A typical beam diameter of 7 mm can be obtained with a divergence below 1°. The beam size can be further restricted by the use of collimating plates down to 0.25 mm in diameter.

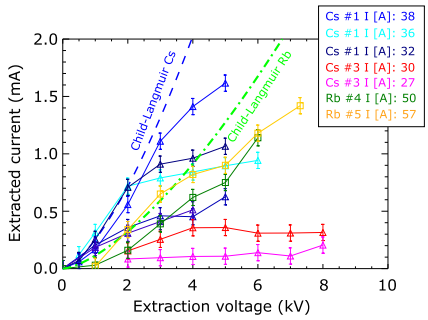

FIG. 2. Extracted current as a function of the extraction voltage for several Cs (triangles) and Rb (squares) sources at different heating currents. The lines represent the space-charge limit given by the Child–Langmuir law for the Cs (blue) and Rb (green) sources.

The injection geometry of the beam was optimized by carrying out simulations of the beam trajectories in order to maximize the diagnostic sensitivity while taking into account the spatial constraints such as the available injection flange and the detector head position, as described in Ref. 19. The final nominal design corresponds to a poloidal injection angle of $\Theta = 0°$ and a toroidal injection angle of $\beta = 4.0°$ (the beam is injected horizontally into the plasma slightly to the right as viewed from the injection port, i.e., into the plane of Fig. 1). The beam trajectories are sensitive to the injection angles. The actual injection angles are calibrated before the experimental campaign. A laser source is placed at the ion source position, and the intersection between the laser beam and planes corresponding to different major radius positions is measured with a laser scanning system that provides a precision of ~1 mm. In order to facilitate the beam alignment and calibration procedure, the beam is mounted on a rail structure, which allows precise positioning of the beam in 3D and gives the possibility of moving the injector to a retracted position during maintenance periods.[20]

B. Detection system

The detection system is composed of an optical head, which is placed at the first wall of sector 13, and the optical system, as shown in Fig. 1(b). The main component of the optical head is a scintillator screen, which acts as the active component of the detection system. A number of scintillator materials have been characterized against irradiation by Cs ions.[34] The TG-Green was selected as the best option and installed at AUG. The scintillator is deposited onto a stainless steel plate of 16.9 × 6 cm^2. The estimated thickness of the scintillator layer is around 250 μm, which is larger than the range of Cs and Rb ions at 100 keV in the material (~30 and 45 nm, respectively). Therefore, it is guaranteed that the ions deposit all their energy in the scintillator material.

The optical head is protected by a tungsten coated graphite heat shield and includes a movable shutter, which is driven by a pneumatic system. The shutter is used to protect the system while there is no operation and also during boronizations. A thermocouple is included to monitor the temperature of the scintillator screen. The temperature of the scintillator screen typically ranges from room temperature at the beginning of the experimental day to several tens of degrees at the end of the experimental day, depending on the

03 November 2026 15:33:44

© Author(s) 2024

auxiliary heating power used during the experiments. Therefore, no deleterious impact on the scintillator yield is expected.[35]

The optical head contains a set of 6 off-the-shelf lenses that act as an objective to create an image of the scintillator plate on an image guide (IG) of size 17 × 7 mm^2. The IG is an array of 1700 × 700 glass fibers with a diameter of 10 μm. Its nominal transmission is ~45% at 550 nm (corresponding to the peak emission of the TG-Green scintillator). The other end of the IG is attached to a viewing port in sector 13, where it is imaged by a CM-030PMCL-RH camera (JAI, Ltd.) with 659 × 494 pixels^2 and a frame rate of up to 120 fps. The first lens is located at a distance of 230 mm from the scintillator, providing an object space numerical aperture of 0.015 and a total transmission of $T(550\text{ nm}) = T_{lenses} \times T_{IG} \sim 0.42$. The optical system is designed to provide, nominally, a spatial resolution better than 200 μm in the whole field of view, which is estimated to be required for the measurement of localized plasma potential fluctuations.[18] The rms spot size ranges from ~5 μm in the center of the image to 60 μm at the edges, and the distortion ranges from 0 at the optical axis up to 11% at the edges. The aperture of the system is controlled by an adjustable iris placed between lenses 3 and 4. It is nominally set to 10.5 mm, but it can be adjusted to increase the numerical aperture at the expense of image resolution.

The performance of the full optical system is assessed before the experimental campaign by calibrating the system resolution and distortion. The system resolution is measured using a resolution test target of type USAF 1951. The target is placed on the plane of the scintillator plate, and an image is taken. This is illustrated in Fig. 3(a). In order to calculate the system resolution, we search for the smallest set of lines that can be distinguished. In our case, this corresponds to group 1 element 6, as shown in Fig. 3(b), which shows the pixel intensity along the red line of 3 (a). This corresponds to a resolution of at least 3.5 lp/mm, which is equivalent to a resolution better than 300 μm in the object space, likely limited by the camera chip size and not the optics.

On the other hand, the distortion of the system is measured by placing a plotting paper with a known grid size of 0.5 cm at the position of the scintillator. Again, an image is taken, and the distortion of the system is calculated as $D = \frac{AD-PD}{PD} \cdot 100$, where AD and PD are the actual and predicted distances of each point to the center of the image, respectively. The result is shown in Fig. 3(c), where the distortion is plotted against the distance to the center of the image.

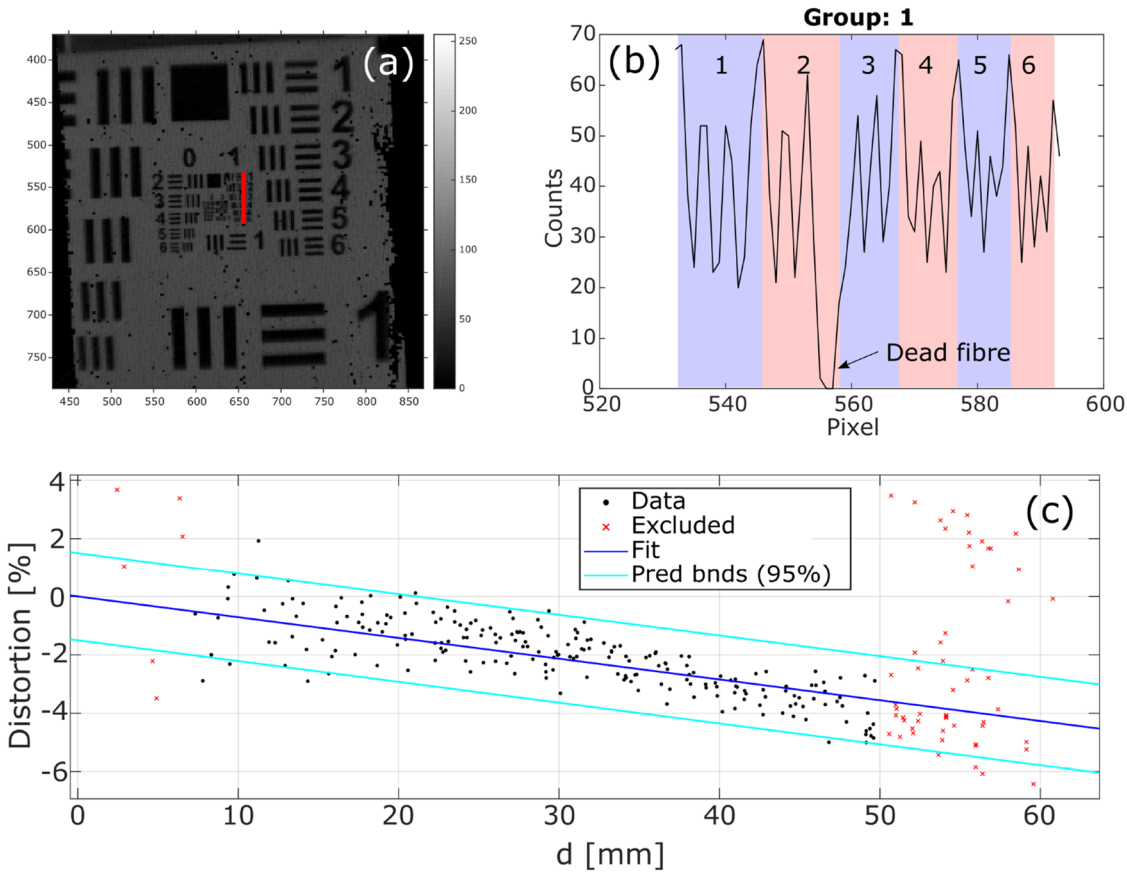

FIG. 3. (a) Camera frame showing the USAF 1951 target used for the calibration. (b) Pixel intensity along group 1, indicated by a red line in (a). (c) Measured distortion of the system.

03 November 2026 15:33:44

© Author(s) 2024

Negative values are obtained, which is indicative of barrel-type distortion. A distortion of 3.7% at a distance of 50 mm from the optical axis is measured, in good agreement with the predicted value of 4%.

III. SENSITIVITY ANALYSIS

In order to correctly interpret the measurements, a set of systematic simulations was performed with the i-HIBPsim code.[37] The sensitivity to global and local electron density and electron and ion temperature fluctuations has been investigated. A comparison has been made between the use of a primary beam of Cs and Rb in order to estimate the expected signal intensity levels. The simulations were performed using plasma discharge No. 34570 at t = 3.53 s as the baseline scenario, with I_p = 0.6 MA and B_t = 2.5 T. In order to systematically change the profiles, the experimental profiles were fitted to the well-known modified hyperbolic tangent function (see, e.g., Ref. 38). The function is defined as

$$f(z) = \frac{a_0 + a_1}{2} + \frac{a_1 - a_0}{2} \cdot \frac{(1 + a_4 z + a_5 z^2 + a_6 z^3)e^z - (1 + a_7 z + a_8 z^2 + a_9 z^3)e^{-z}}{e^z + e^{-z}},$$

where $z = \frac{a_2 - x}{a_3}$. The parameters of this analytical fit allow us to modify almost independently the different regions of the profiles such as the pedestal location, the pedestal height, the scrape-off layer (SOL) values, or the core values, as shown in Fig. 4. A primary beam of ^{85}Rb at 70 keV is considered in the simple thin-beam approximation for these simulations. Electron impact ionization reactions were considered for the attenuation of the primary and secondary beams, while charge exchange reactions were additionally considered for the attenuation of the primary beam. Charge exchange reactions were neglected for the attenuation of the secondary beam due to the low neutral deuterium density, which is typically below 10^{16} m^{-3} in AUG.[39] No radial electric field nor toroidal magnetic field ripple were included in the simulations for simplicity. The scintillator yield has not been considered in the simulations, and thus, the output provides the ion flux at the scintillator detector only. The result of the simulation for this baseline case is shown in Fig. 5(a). Here, the expected strike line at the scintillator plate is represented, where the color indicates the incident ion flux. Each point along the strike line corresponds to a position along the secondary beam birth profile. Therefore, a mapping between the scintillator strike-position and plasma volume can be performed. In the following, the results of global and local variations of the density and temperature profiles are discussed.

A. Sensitivity to density profile variations

The sensitivity scans in density are performed by varying the density profile while keeping the same temperature profiles. We consider first global variations of the density profile by changing the parameter a_1 from −30% to +30%, which controls the pedestal top value. The resulting profiles are shown in Fig. 5(b). It can be seen that the effect is to increase/decrease the pedestal top density and the core profile accordingly, in this case ranging from 2×10^{19} to 5×10^{19} m^{-3} on the axis. The results are shown in Fig. 5(c), where the secondary beam ion density profile reaching the detector plate as a function of the radius at the birth location is plotted for different values of the parameter a_1. The baseline signal level (corresponding to the nominal value of a_1) is ~100 mA/m^2. It can be seen that the global variation of the profile has a clear impact on the expected signal level, ranging from a signal decrease of −36% for the high density cases to a signal increase of 11% (at the separatrix) for the low density cases. While the changes in the SOL density profile also have an impact on the signals, the overall decrease of the signal is dominated by the increase of the density profile at the pedestal and further inward. This has been checked in simulations (not shown here) where only the SOL density profile is changed by scanning the parameter a_0. These simulations show a more moderate impact on the overall signal level. Instead, they show a clear change in the profile shape of the secondary beam ion density reaching the detector plate. Therefore, it should be noted that the resulting intensity pattern in the scintillator is an apriori complex non-linear function of the density and temperature profiles. The resulting structure is a competition between the secondary beam birth intensities and the attenuation of the primary and secondary beams. In all these cases, the signal peaks around the separatrix position.

Local density variations have been considered by adding a density perturbation of Gaussian shape at the pedestal top, separatrix, and scrape-off layer (SOL) positions. The resulting profiles are illustrated in Figs. 6(a)–6(c), where realistic perturbation amplitudes up

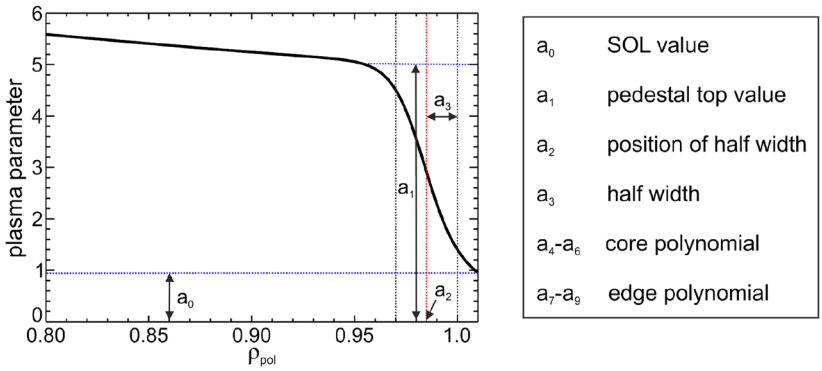

FIG. 4. Modified hyperbolic tangent. Adapted from Ref. 36.

03 November 2026 15:33:44

© Author(s) 2024

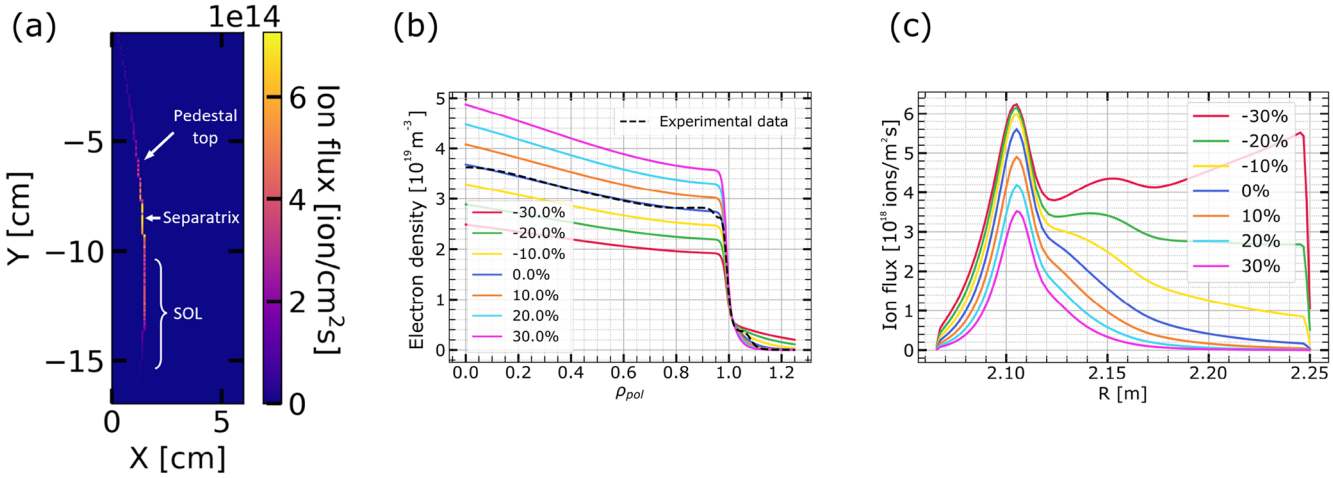

FIG. 5. (a) Synthetic strike line at the scintillator plate. (b) Input density profiles for different values of the pedestal top density defined by the parameter a_1. Variation is given in percentages relative to the nominal value. (c) The resulting intensity profile along the strike line as a function of the secondary beam birth position and the parameter a_1.

to 15%, 30%, and 90% have been considered, respectively. These correspond to typical values reported in the literature for different instabilities such as geodesic acoustic modes (GAMs)[40] or staircases[41] inside the pedestal top, edge localized modes (ELMs) at the plasma edge,[42] and scrape-off layer filaments,[43] among others. The resulting intensity patterns at the scintillator are shown in Figs. 6(d)–6(f), as a function of the secondary beam birth radial location, where a mapping between the scintillator strike-points and the plasma volume has been performed as described earlier. The effect is relatively weak for the perturbations at the pedestal top and separatrix positions, where the maximum variation in the expected ion flux is observed at the mapped pedestal top position to be 10% and 30%, respectively. However, perturbations in the scrape-off layer seem to have a much more drastic effect. As the amplitude of the

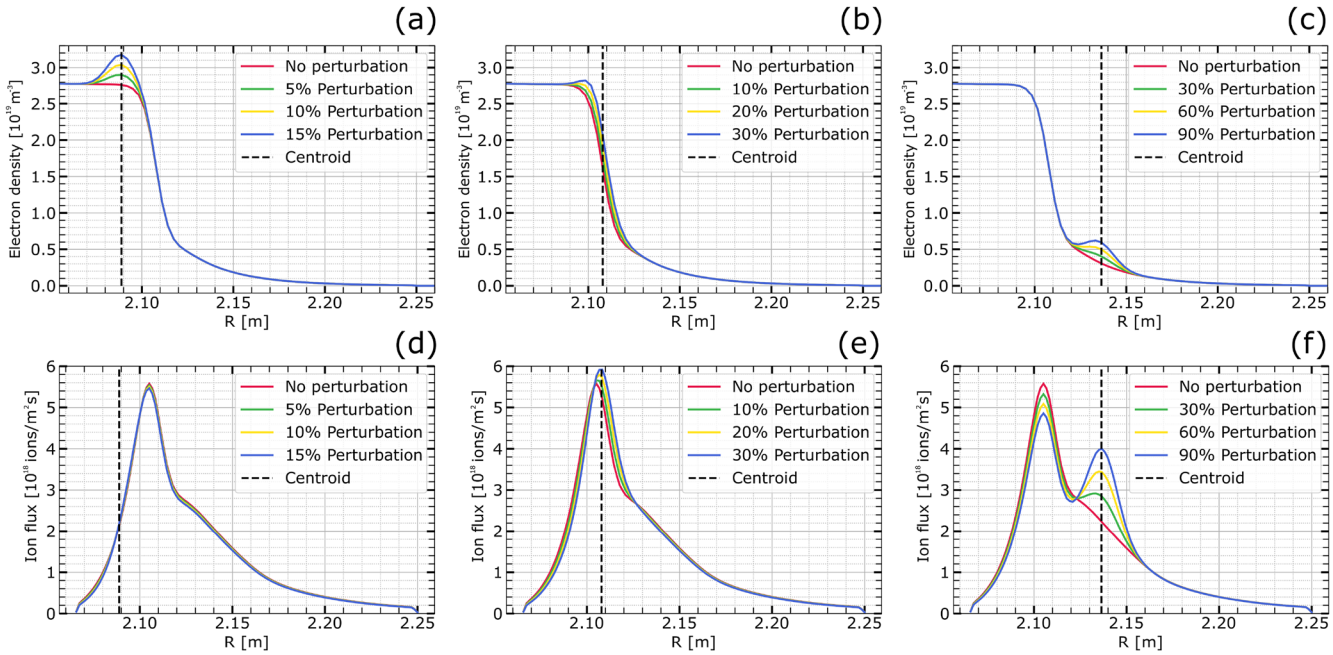

FIG. 6. Input density profiles for perturbations at (a) pedestal top, (b) separatrix, and (c) scrape-off layer. The resulting intensity profiles along the strike line are shown in (d)–(f).

03 November 2026 15:33:44

© Author(s) 2024

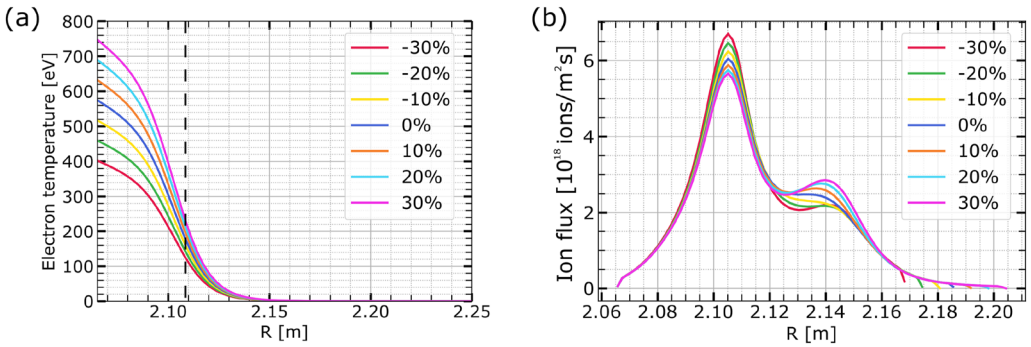

FIG. 7. (a) Input electron temperature profiles for different values of the parameter a_1. The variation is given in percentages relative to the nominal value. (b) The resulting intensity profile along the strike line as a function of the secondary beam birth position and the parameter a_1.

perturbation is increased, the intensity of the main peak in the scintillator signal decreases, while a second peak at the radial position of the perturbation emerges, leading to a double-peak structure. Therefore, it is concluded that the diagnostic is more sensitive to density perturbations in the scrape-off layer. Note that density perturbations of up to 100% in the scrape-off layer are not unrealistic and could be expected for phenomena such as filaments.[44,45]

B. Sensitivity to temperature profile variations

The analogous procedure is repeated for the electron temperature profile while keeping the ion temperature profile and the electron density profile constant. First, we consider global T_e variations by scanning parameter a_1, as shown in Fig. 7(a). The resulting intensity pattern at the scintillator plate is shown in Fig. 7(b). In this case, it can be seen that the expected intensity variation at the scintillator plate ranges only from −11% to 28% at the mapped separatrix position, even when we consider temperature variations that go from 100 to 200 eV at the separatrix. Local variations of T_e are also evaluated following the same approach as before. This is illustrated in Fig. 8. Again, it can be seen that the resulting intensity changes at the scintillator plate remain below 10%, even when considering unrealistic temperature perturbations of up to 60% and 50% in the separatrix and pedestal top, respectively. Therefore, it is concluded that the diagnostic is mostly unsensitive to variations in the electron temperature.

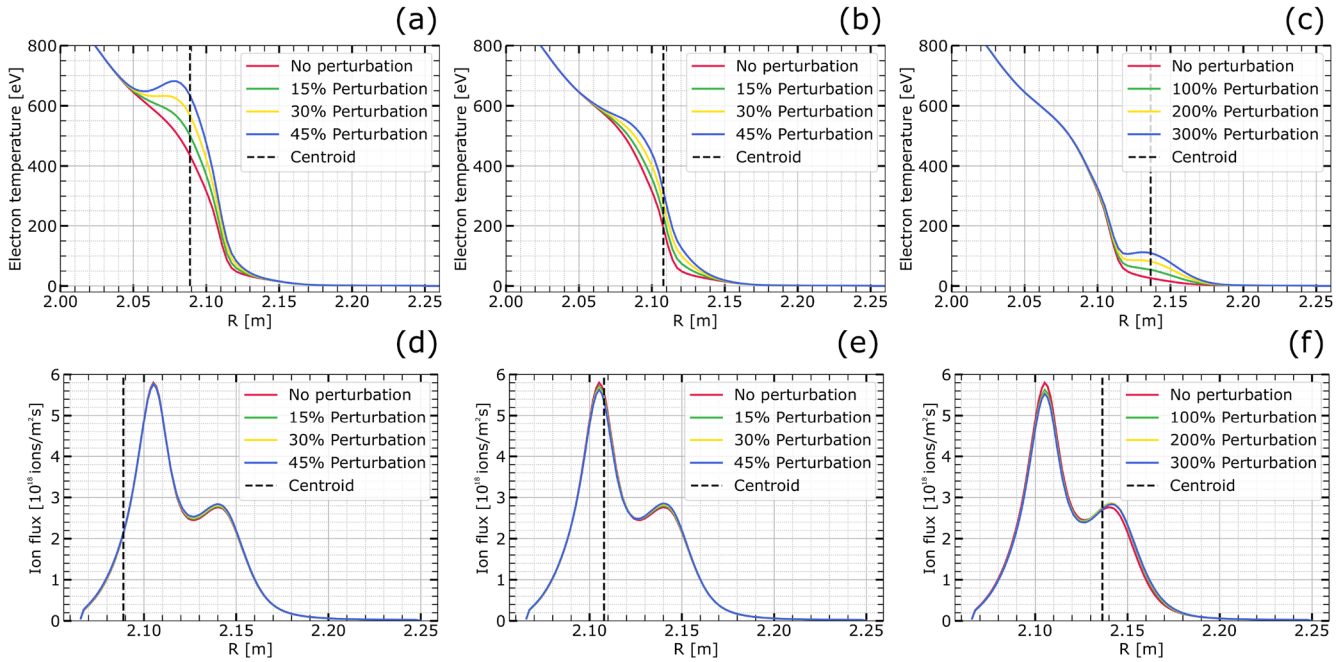

FIG. 8. Input profiles for electron temperature perturbations at (a) pedestal top, (b) separatrix, and (c) scrape-off layer. The resulting intensity profiles along the strike line are shown in (d)–(f).

03 November 2026 15:33:44

© Author(s) 2024

The same approach has been followed for the ion temperature profiles (not shown here). Changes in T_i only affect the attenuation of the secondary beams by entering into the reaction rates of the charge exchange reactions. The result is similar as for T_e variations, and changes below 1% in the signal intensity are obtained even for unrealistic temperature variations of up to 40%.

C. Cs vs Rb beam

Simulations are carried out to compare the expected intensity levels when using a Cs and a Rb beam. In this case, not only the species are changed, but also the energy of the primary beam. Due to the higher mass of Cs, the energy of the primary beam needs to be reduced in order to match the trajectory of the secondary beams so that they reach the detector. In zeroth-order approximation, this is given by the Larmor radius of the ions. A Rb beam at 70 keV and a Cs beam at 50 keV are considered for this comparison, where different density profiles have been used by varying parameter a_1.

The results are shown in Fig. 9, where in (a), the secondary beam density expected at the scintillator is plotted against the different values of the parameter a_1, in red for Cs and in blue for Rb. It can be seen that the expected signals for the Cs beam are lower by at least one order of magnitude. In (b), the secondary beam birth densities at R = 2.10 m (which corresponds to the peak of the signal at the scintillator plate) are shown. In this case, the birth density levels are similar for both species, suggesting that the overall lower signal levels expected at the scintillator plate are due to a stronger attenuation of the secondary beams. The effect is twofold: first, the reaction rates for electron impact ionization and charge exchange reactions, which dominate the secondary beam attenuation, are larger for Cs than for Rb, as shown in Fig. 10; second, the velocity of the particles is much higher for the case of Rb, mainly due to its lower mass but additionally due to the higher primary beam energies needed. The beam attenuation at a certain position l_0 along the beam trajectory is generally given by[18,19]

$$j_b(l_0) = j_b(0)\exp\left\{-\frac{1}{v_b}\int_0^{l_0}\sum_k n_e\langle\sigma v\rangle_k dl\right\}, \quad (2)$$

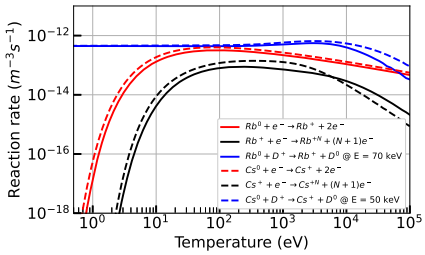

FIG. 10. Reaction rates for Cs (dashed line) and Rb (full line). Primary beam electron impact ionization is shown in red. The secondary beam electron impact ionization is shown in black. The charge exchange reaction is shown in blue.

where j represents the current density, v_b is the beam velocity, n_e is the plasma electron density, l is the distance along the beam trajectory, and $\langle\sigma v\rangle_k$ is the reaction rate of all relevant k reactions. Therefore, a higher beam velocity leads to lower primary beam attenuation, in principle facilitating deeper beam deposition in the plasma and, more importantly, lower secondary beam attenuation. It is, therefore, concluded that the use of the Rb beam against the Cs beam should be favorable in terms of the expected secondary ion flux at the scintillator plate.

IV. COMMISSIONING AND FIRST SIGNALS

The diagnostic went into operation for the first time during the experimental campaign 2020–2021 at AUG. In this campaign, Cs was used as a probe beam. The injector and detection systems performed correctly. However, no signal was obtained. It was decided to change the ion source to Rb in the 2021–2022 campaign since modeling predicted higher signal levels due to a lower secondary beam attenuation in the plasma (see Sec. III C for more details). The first signals were then observed in the scintillator. In the following, the main characteristics of the signals are discussed.

A. First signals and operational space

The typical signals obtained, in the absence of any collimating plate, consist of a strike line of ~3 cm width and 12 cm height. An

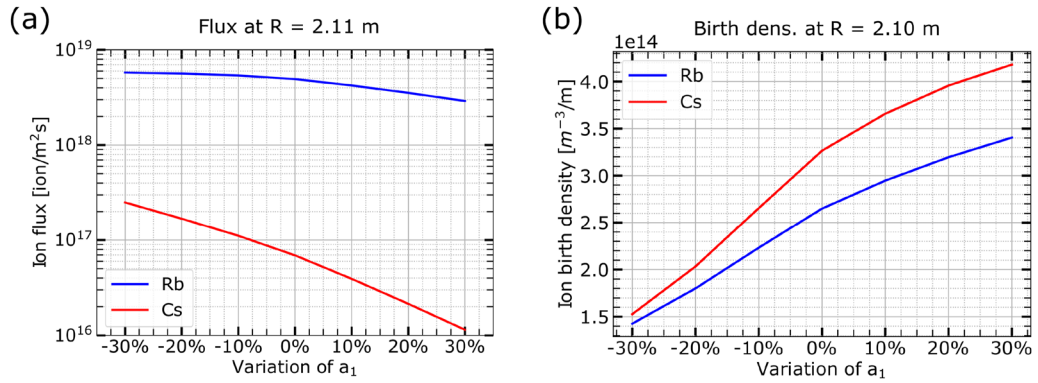

FIG. 9. Comparison between the Rb beam at 70 keV and the Cs beam at 50 keV for different density profiles. (a) Ion flux at the scintillator plate as a function of parameter a_1. (b) Secondary beam ion birth density as a function of parameter a_1.

03 November 2026 15:33:44

© Author(s) 2024

example is shown in Fig. 11(b). As described in Refs. 18 and 37, the width of the strike line is linked to the beam properties (beam width, divergence, etc.), while the height is related to the ionization volumes of the probe beam. Different positions along the strike line height [vertical direction in Fig. 11(b)] correspond to different radial positions in the plasma. Signals have been obtained for plasmas with plasma current ranging from 0.2 to 0.8 MA, on-axis magnetic fields ranging from 1.9 to 2.7 T, and injection energies between 60 and 72 keV, as shown in Fig. 12. This database includes 41 time windows for which signals have been observed on the scintillator plate. The shadowed gray region indicates the target region of operation, including the reference scenarios that had been used in the design phase. However, it is important to notice that all these points correspond to cases in which the line-averaged density, as measured by the central interferometer chord, is below 2.0–3.0 × 10^{19} m^{-3}. These all correspond to L-mode plasmas. In view of the simulation results presented in Sec. III, this density threshold is attributed to the attenuation of the secondary beam. The fact that measurements have only been obtained for Rb beams and not for Cs is also consistent with the simulation results.

However, during the operation, several challenges had to be faced. One of the first observations was that stray light from the plasma could contaminate the signal. This can complicate the analysis of the signals, especially in H-mode plasmas with edge-localized modes. As a solution, an optical filter centered at 540 nm with a bandwidth of 80 nm was used in front of the camera. This way, although there is still some stray light going into the system, a large fraction of it is filtered out and the signal-to-background ratio (SBR) is improved up to values of 2–5 depending on the case, where the SBR is defined as $SBR = \frac{\langle ROI_{beam} \rangle}{\langle ROI_{background} \rangle}$, where $\langle ROI_{beam} \rangle$ and $\langle ROI_{background} \rangle$ are the average pixel counts inside a region of interest (ROI) in the camera frame containing the beam signal and no beam signal (background only), respectively. A comparison of the signal with and without a filter is shown in Fig. 11, where two frames corresponding to matching plasma conditions of I_p = 0.35 MA, B_t = 2.5 T, and density have been selected. Additionally, two frames from a beam modulation experiment are shown in Figs. 11(c) and 11(d), comparing a beam-on phase and a beam-off phase, respectively. The beam pattern can be clearly distinguished, while in the beam-off phase, the scintillator is still visible due to the stray light. A weak footprint of the beam is still visible at the center of the scintillator due to the relatively long exposure time of the camera, which makes it impossible to capture a complete phase with the beam off.

An additional constraint came from the effect of neutron irradiation on the image guide (IG). It is well known that glass fiber optics exposed to high neutron flux suffer a reduction in their transmissivity.[46] This effect is observed in this experimental setup, as illustrated in Fig. 13. The transmission curve of the IG as a function of the wavelength is measured before (black) and after (blue) the 2021 campaign. At the central emission wavelength of the scintillator, λ = 550 nm, the transmission is reduced from 45% to below 5%. The transmission is recovered after two heating cycles (performed ex-vessel) up to 220 °C, as shown in red and magenta. This proce-

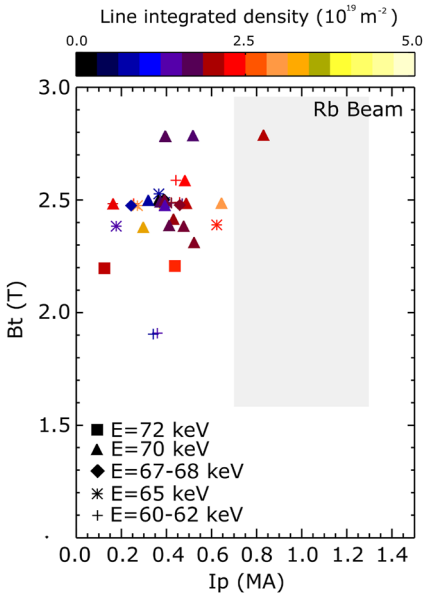

FIG. 12. Parameter space of the i-HIBP operation using a Rb beam. Each point corresponds to a time window during which a signal has been detected on the scintillator plate. The color code represents the maximum line integrated density at the plasma during the corresponding time window. Different symbols correspond to different primary beam energies. The gray-shaded region represents the target scenarios for which the diagnostic was designed.

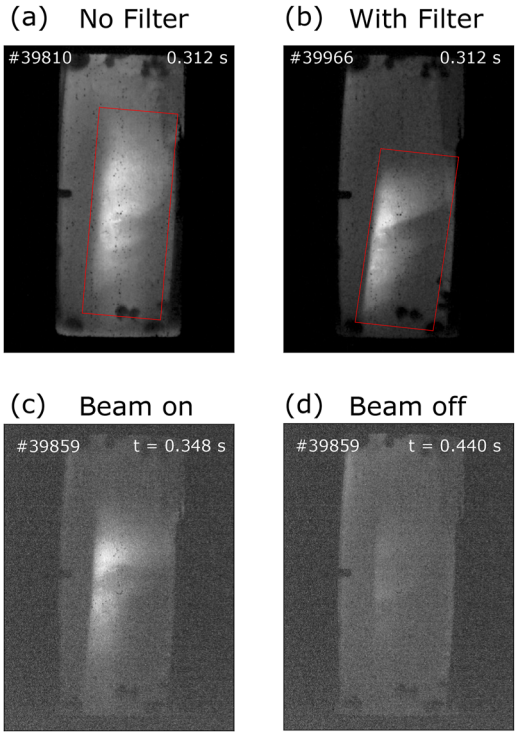

FIG. 11. Raw frames showing the signal measured at the scintillator in a case without (a) and with (b) an optical filter. The red rectangle indicates the area in which the beam footprint is observed. (c) and (d) show frames corresponding to phases with the iHIBP beam on and off, respectively, in a beam modulation experiment.

03 November 2026 15:33:44

© Author(s) 2024

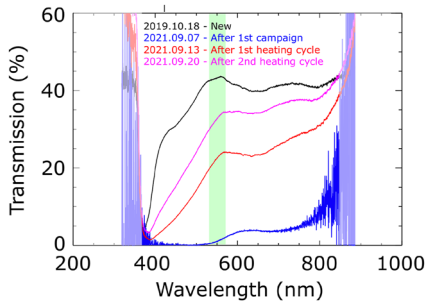

FIG. 13. Transmission of the image guide as a function of the wavelength before (black) and after (blue) the experimental campaign, showing a clear degradation. The transmission is partially healed after the first (red) and second (magenta) heating cycles (ex-vessel). The shadowed green region indicates the peak of the TG-Green emission spectrum, approximately.

dure allows us to recover the IG transmission in-between campaigns, whenever access to the vessel is granted. Since the IG is installed in-vessel, there is no possibility to exchange the IG within the campaign whenever the transmission is considered to be too low. In order to alleviate this problem, an in-vessel heating system for the IG has been developed. In the in-vessel setup, at high temperatures, some outgassing is observed. Therefore, the allowed baking temperatures are limited to lower values for machine safety reasons. Therefore, in this case, the recovery of the IG transmission is only up to 10%, which is still a factor x2–x5 increase compared to the unhealed IG, as shown in Fig. 13 (blue curve).

A third obstacle has been found during operation, which is related to beam deflection due to a stray magnetic field at the injector beamline. The injector is designed to shield the stray magnetic field in two phases. First, the structural steel is expected to reduce the stray field from ~50–1 mT. Second, by including the inner cylinders of a μ metal foil, the magnetic field is expected to drop below 0.2 mT.[33] However, during operation, a shift of the beam of ~4 mm (instead of 0.3 mm, expected by design) at the diagnostic chamber and 7 mm at the injector port is observed. Based on these displacements, a stray magnetic field of up to 2 mT is estimated at the injector beamline, suggesting that the magnetic shielding concept is not performing as expected. This is tolerable when the beam is fired without adding a collimation plate to the diagnostic chamber. However, adding such collimation plates leads to the complete blocking of the beam due to the 4 mm shift, which moves the beam out of the collimation path. Therefore, in practice, it is not yet

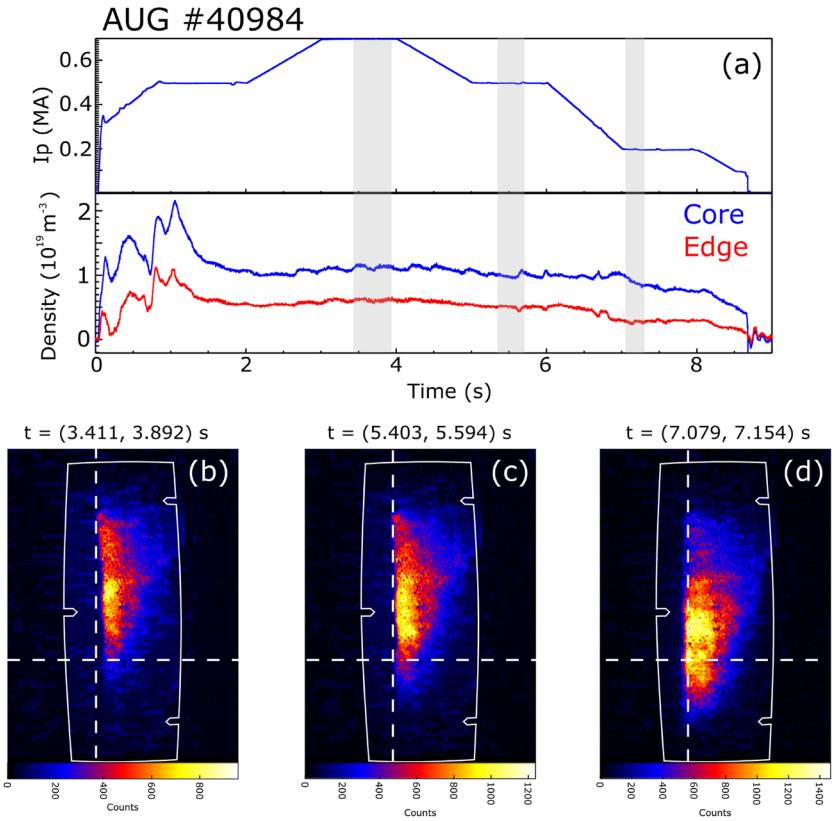

FIG. 14. (a) Overview of plasma discharge No. 40984. The top panel shows the evolution of the plasma current. The bottom panel shows the plasma density measured by two different interferometer chords. (b)–(d) show the measured signal in the scintillator plate at three different time windows corresponding to a plasma current of 0.7, 0.5, and 0.2 MA, respectively.

03 November 2026 15:33:44

© Author(s) 2024

possible to collimate the beam, which would be desirable to achieve a smaller width of the scintillator strike line for more precise deflection measurements.

Currently, the low SBR limits the capabilities of the diagnostic. Higher SBR would allow faster measurements, which would enable the study of many physics phenomena as discussed in Sec. I. Therefore, in order to overcome the limitations discussed earlier and increase the signal level, several actions are being considered for future campaigns:

1. The use of a lighter species such as K should be beneficial in terms of secondary beam attenuation and scintillator yield. The performance of a K source will be investigated, and simulations will be carried out to determine if, from the beam trajectory point of view, the use of K is an alternative given the high voltage limits of the current setup.
2. Improvement of the optical system: the possibility of using a full optical system (avoiding the use of an image guide) is being evaluated to avoid the problem of image guide degradation.
3. Improvement of the primary beam current density by using a single-step electrostatic focusing system.
4. Improvement of the magnetic shielding of the beamline by adding more shielding material in order to facilitate beam collimation, as well as alternative collimation schemes. Another alternative would be to minimize the stray magnetic field at the beamline by using specific coil configurations (e.g., minimizing the current of the nearby poloidal field coils responsible for the high stray field at the beamline).
5. The use of alternative scintillator materials is being investigated, with the goal of finding a material with slower

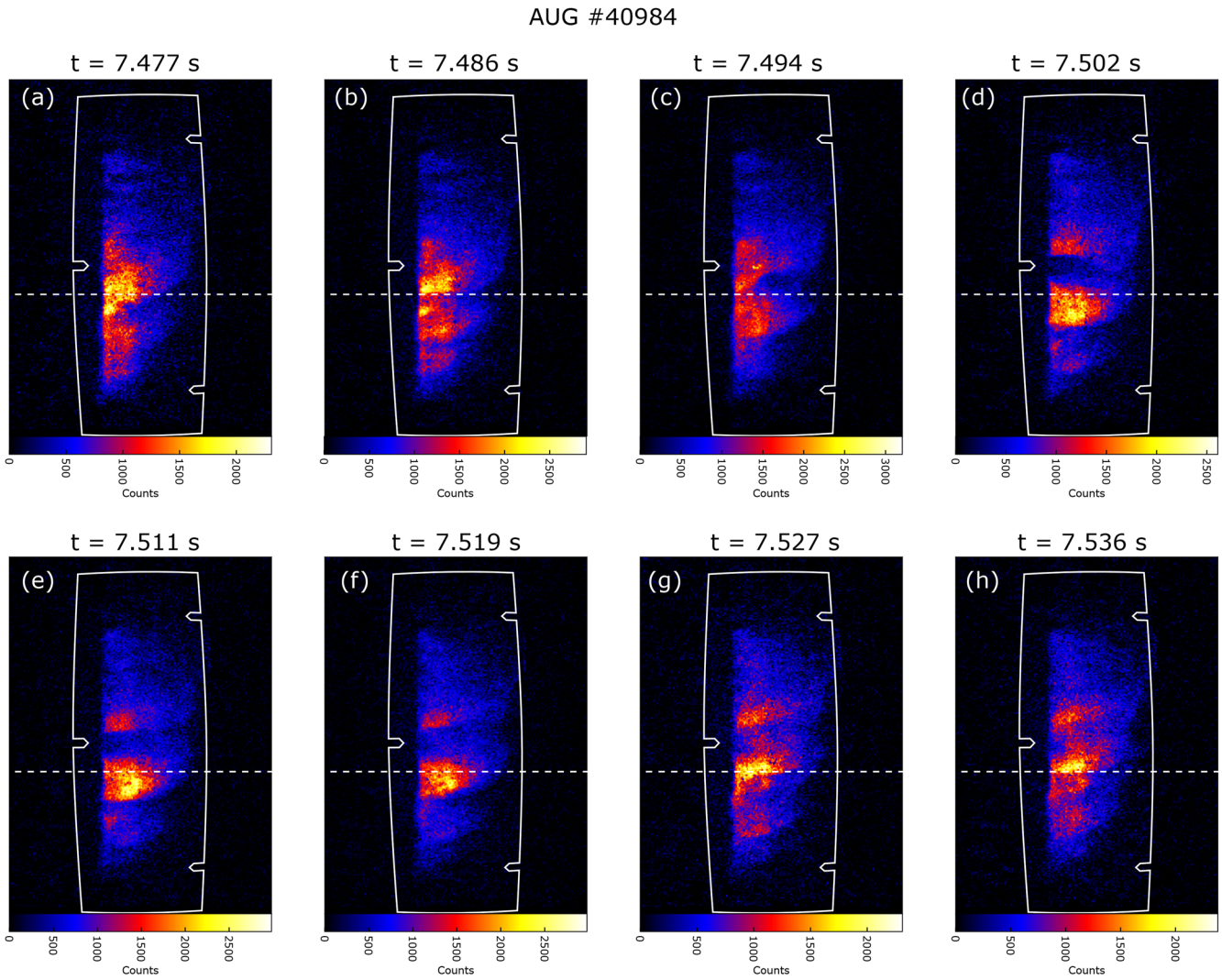

FIG. 15. (a)–(h) Sequence of consecutive frames measured in AUG plasma discharge No. 40984. The signal features a complex structure with multiple peaks moving in a vertical direction.

03 November 2026 15:33:44

© Author(s) 2024

degradation while keeping the requirements on photon yield and decay time.

B. Scans in I_p

In order to test the proof-of-principle of the diagnostic, measurements have been carried out at different plasma currents, where a displacement of the whole strike line is expected due to changes in the poloidal magnetic field. An example is shown in Fig. 14(a) for plasma discharge No. 40984, where three phases with a plasma current of 0.7, 0.5, and 0.2 MA are obtained. The corresponding strike line pattern at each of these phases is shown in (b)–(d), respectively, where several frames have been integrated for each case. It can be seen that the edge of the strike-pattern is shifted toward the left by a distance of 5 mm, corresponding to a displacement of 1.1 cm/MA.

C. Intensity signal dynamics

The measured intensity pattern along the strike line is now discussed. In steady-state conditions, the i-HIBPsim simulations discussed in Sec. III indicate that an intensity distribution with a single peak at approximately the separatrix is to be expected. Figure 14(d) shows the time integrated signal in plasma discharge No. 40984 between 7.079 and 7.154 s, corresponding to a steady-state phase with $I_p = 0.2$ MA and a line averaged density of 0.8×10^{19} m^{-3}. Indeed, the intensity map resembles an intensity distribution with a single peak.

However, the instantaneous distributions, as measured by consecutive frames within the same time window, show a more complex intensity map. This is illustrated in Figs. 15(a)–15(h). Instead of a single peak distribution, multiple peak structures are observed. The peaks appear to be displaced, which is better observed by comparison with the horizontal white dashed lines that are included for reference. This multiple peak structure appears to be consistent with the expected distributions from density perturbations in the SOL region as obtained in the simulations from Sec. III, suggesting that the diagnostic may be sensitive to changes in the profile structure at the SOL and plasma edge.

V. SUMMARY

The first measurements of an imaging heavy-ion beam probe at ASDEX Upgrade have been obtained. The measurements have been successful only when using an Rb beam with energies between 60 and 72 keV, plasma current between 0.2 and 0.8 MA, and magnetic fields between 1.9 and 2.7 T. The proof-of-principle of the diagnostic has been established. Different plasma currents lead to deviations from the strike-pattern as predicted. These deflections, due to changes in the toroidal plasma current, could be potentially used to reconstruct the local current density at the edge. The appearance of multiple peak structures, consistent with variations in the SOL density, shows the potential of the diagnostic to measure density fluctuations. Furthermore, the temporally averaged intensity along the strike line could be used to reconstruct the density profile at the edge, which will be the subject of a future publication. The diagnostic performs as expected in terms of spatial resolution, provided that no collimator plates have been used yet. The most limiting factor appears to be the low intensity of the signals, which is attributed mostly to the attenuation of the secondary beams. A threshold is found in the line integrated density of the central interferometer chord of $2.0–3.0 \times 10^{19}$ m^{-2}, and measurements have been possible only in low density L-mode plasmas. The time resolution of the diagnostic is limited by the signal-to-background ratio, which at the current stage also limits the potential of the diagnostic. Furthermore, modifications to the system to increase the signal-to-background ratio are discussed, including the use of different beam species and scintillator materials, the modification of the optical system, and the magnetic shielding of the beam and its focusing capabilities.

ACKNOWLEDGMENTS

This work has been carried out within the framework of the EUROfusion Consortium, funded by the European Union via the Euratom Research and Training Program (Grant Agreement No. 101052200—EUROfusion). The views and opinions expressed are, however, those of the author(s) only and do not necessarily reflect those of the European Union or the European Commission. Neither the European Union nor the European Commission can be held responsible for them. This work has been supported by the Helmholtz Association under Grant No. VH-NG-1350, by the European Research Council (ERC) under the European Union's Horizon 2020 research and innovation program Grant No. 805162 and by the European Union under Marie Sklodowska Curie Grant Agreement No. 101069021.

AUTHOR DECLARATIONS

Conflict of Interest

The authors have no conflicts to disclose.

Author Contributions

J. Galdon-Quiroga: Conceptualization (equal); Data curation (equal); Formal analysis (equal); Investigation (equal); Methodology (equal); Software (supporting); Writing – original draft (lead); Writing – review & editing (lead). **G. Birkenmeier**: Conceptualization (equal); Data curation (equal); Formal analysis (equal); Investigation (equal); Methodology (equal); Project administration (lead); Resources (lead); Supervision (lead); Writing – review & editing (supporting). **P. Oyola**: Data curation (equal); Formal analysis (equal); Investigation (equal); Software (lead). **H. Lindl**: Data curation (equal); Investigation (equal). **A. Rodriguez-Gonzalez**: Data curation (equal); Investigation (equal). **G. Anda**: Conceptualization (equal); Funding acquisition (supporting); Investigation (supporting); Resources (equal); Supervision (supporting). **M. Garcia-Munoz**: Conceptualization (equal); Data curation (supporting); Funding acquisition (supporting); Resources (supporting); Software (supporting); Supervision (supporting). **A. Herrmann**: Investigation (supporting); Methodology (equal); Project administration (supporting); Resources (equal). **J. Kalis**: Data curation (supporting); Funding acquisition (equal); Investigation (supporting); Project administration (equal); Resources

03 November 2026 15:33:44

© Author(s) 2024

(supporting); Supervision (supporting). **K. Kaunert**: Data curation (supporting); Investigation (supporting); Methodology (equal); Resources (supporting). **T. Lunt**: Investigation (supporting); Resources (supporting); Software (supporting). **D. Refy**: Data curation (supporting); Investigation (supporting); Resources (supporting); Software (supporting). **V. Rohde**: Conceptualization (supporting); Funding acquisition (supporting); Methodology (supporting); Resources (supporting). **J. Rueda-Rueda**: Data curation (supporting); Methodology (equal); Project administration (supporting); Resources (equal); Software (supporting). **M. Sochor**: Investigation (supporting); Methodology (equal); Resources (supporting). **B. Tal**: Data curation (supporting); Investigation (equal); Methodology (equal); Resources (supporting); Software (supporting); Writing – review & editing (supporting). **M. Teschke**: Methodology (supporting); Resources (supporting). **M. Videla**: Investigation (supporting); Methodology (supporting); Resources (supporting). **E. Viezzer**: Data curation (supporting); Funding acquisition (equal); Investigation (equal); Methodology (equal); Project administration (equal); Resources (supporting); Supervision (supporting); Writing – review & editing (supporting). **S. Zoletnik**: Conceptualization (supporting); Funding acquisition (supporting); Methodology (supporting); Resources (supporting).

DATA AVAILABILITY

The data that support the findings of this study are available from the corresponding author upon reasonable request.

REFERENCES

[1] P. M. Schoch, A. Carnevali, K. A. Conner, T. P. Crowley, J. C. Forster, R. L. Hickok, J. F. Lewis, J. G. Schatz, and G. A. Hallock, "Heavy-ion beam probe diagnostic systems (invited)," Rev. Sci. Instrum. **59**, 1646–1651 (1988).

[2] T. P. Crowley, "Rensselaer heavy ion beam probe diagnostic methods and techniques," IEEE Trans. Plasma Sci. **22**, 291–309 (1994).

[3] A. V. Melnikov, L. I. Krupnik, L. G. Eliseev, J. M. Barcala, A. Bravo, A. A. Chmyga, G. N. Deshko, M. A. Drabinskij, C. Hidalgo, P. O. Khabanov, S. M. Khrebtov, N. K. Kharchev, A. D. Komarov, A. S. Kozachek, J. Lopez, S. E. Lysenko, G. Martin, A. Molinero, J. L. De Pablos, A. Soleto, M. V. Ufimtsev, V. N. Zenin, and A. I. Zhezhera, "Heavy ion beam probing—Diagnostics to study potential and turbulence in toroidal plasmas," Nucl. Fusion **57**, 072004 (2017).

[4] A. Fujisawa, K. Itoh, H. Iguchi, K. Matsuoka, S. Okamura, A. Shimizu, T. Minami, Y. Yoshimura, K. Nagaoka, C. Takahashi, M. Kojima, H. Nakano, S. Ohsima, S. Nishimura, M. Isobe, C. Suzuki, T. Akiyama, K. Ida, K. Toi, S.-I. Itoh, and P. H. Diamond, "Identification of zonal flows in a toroidal plasma," Phys. Rev. Lett. **93**, 165002 (2004).

[5] P. M. Schoch, K. A. Connor, D. R. Demers, and X. Zhang, "Zonal flow measurements using a heavy ion beam probe," Rev. Sci. Instrum. **74**, 1846–1849 (2003).

[6] A. Fujisawa, K. Itoh, A. Shimizu, H. Nakano, S. Ohshima, H. Iguchi, K. Matsuoka, S. Okamura, T. Minami, Y. Yoshimura, K. Nagaoka, K. Ida, K. Toi, C. Takahashi, M. Kojima, S. Nishimura, M. Isobe, C. Suzuki, T. Akiyama, Y. Nagashima, S.-I. Itoh, and P. H. Diamond, "Experimental evidence of a zonal magnetic field in a toroidal plasma," Phys. Rev. Lett. **98**, 165001 (2007).

[7] T. Ido, K. Kamiya, Y. Miura, Y. Hamada, A. Nishizawa, and Y. Kawasumi, "Observation of the fast potential change at L-H transition by a heavy-ion-beam probe on JFT-2M," Phys. Rev. Lett. **88**, 055006 (2002).

[8] T. Kobayashi, K. Itoh, T. Ido, K. Kamiya, S.-I. Itoh, Y. Miura, Y. Nagashima, A. Fujisawa, S. Inagaki, K. Ida, and K. Hoshino, "Spatiotemporal structures of edge limit-cycle oscillation before L-to-H transition in the JFT-2M tokamak," Phys. Rev. Lett. **111**, 035002 (2013).

[9] A. Melnikov, L. Eliseev, R. Jiménez-Gómez, E. Ascasibar, C. Hidalgo, A. Chmyga, A. Komarov, A. Kozachok, I. Krasilnikov, S. Khrebtov, L. Krupnik, M. Liniers, S. Lysenko, V. Mavrin, J. de Pablos, M. Pedrosa, S. Perfilov, M. Ufimtsev, T. Ido, K. Nagaoka, S. Yamamoto, Y. Taschev, A. Zhezhera, and A. Smolyakov, "Internal measurements of Alfvén eigenmodes with heavy ion beam probing in toroidal plasmas*," Nucl. Fusion **50**, 084023 (2010).

[10] S. Ohshima, A. Fujisawa, A. Shimizu, H. Nakano, H. Iguchi, Y. Yoshimura, K. Nagaoka, T. Minami, M. Isobe, S. Nishimura, C. Suzuki, T. Akiyama, C. Takahashi, M. Takeuchi, T. Ito, T. Watari, R. Kumazawa, S.-I. Itoh, K. Itoh, K. Matsuoka, and S. Okamura, "Zonal flow driven by energetic particle during magneto-hydro-dynamic burst in a toroidal plasma," Plasma Phys. Controlled Fusion **49**, 1945 (2007).

[11] T. Ido, K. Itoh, M. Osakabe, M. Lesur, A. Shimizu, K. Ogawa, K. Toi, M. Nishiura, S. Kato, M. Sasaki, K. Ida, S. Inagaki, S.-I. Itoh, and LHD Experiment Group, "Strong destabilization of stable modes with a half-frequency associated with chirping geodesic acoustic modes in the large helical device," Phys. Rev. Lett. **116**, 015002 (2016).

[12] J. A. C. Cabral, A. Malaquias, A. Praxedes, W. V. van Toledo, and C. A. F. Varandas, "The heavy ion beam diagnostic for the tokamak ISTTOK," IEEE Trans. Plasma Sci. **22**, 350–358 (1994).

[13] J. A. Beckstead, S. C. Aceto, T. P. Crowley, D. Demers, P. E. McLaren, A. Ouroua, J. G. Schatz, and P. M. Schoch, "A spatial detector array for measuring plasma turbulence with the heavy ion beam probe," Rev. Sci. Instrum. **68**, 328–331 (1997).

[14] A. Melnikov, "Evolution of heavy ion beam probing from the origins to study of symmetric structures in fusion plasmas," Symmetry **13**, 1367 (2021).

[15] H. Nakano, A. Fujisawa, A. Shimizu, S. Ohshima, H. Iguchi, Y. Yoshimura, and T. Minami, "Reconstruction method of local density fluctuation for heavy ion beam probe measurements," Rev. Sci. Instrum. **78**, 063502 (2007).

[16] A. Fujisawa, M. Kitazawa, A. Shimizu, S. Ohshima, and H. Iguchi, "Prescription for density profile reconstruction using a heavy ion beam probe," Rev. Sci. Instrum. **74**, 3335–3340 (2003).

[17] A. Shimizu, A. Fujisawa, S. Ohshima, H. Nakano, T. Minami, M. Isobe, S. Okamura, and K. Matsuoka, "Density profile measurement with a heavy ion beam probe in a toroidal plasma of the compact helical system," Rev. Sci. Instrum. **89**, 113507 (2018).

[18] J. Galdon-Quiroga, J. Rivero-Rodriguez, M. Garcia-Munoz, G. Birkenmeier, E. Viezzer *et.al.*, "Conceptual design of a scintillator based imaging heavy ion beam probe for the ASDEX upgrade tokamak," J. Instrum. **12**, C08023 (2017).

[19] G. Birkenmeier, J. Galdon-Quiroga, V. Olevskaia, M. Sochor, K. Kaunert, G. Anda, D. Nagy, S. Zoletnik, A. Herrmann, V. Rohde, E. Wolfrum, K. Bald, J. F. Rivero-Rodriguez, E. Viezzer, and M. Garcia-Munoz, "Beam modelling and hardware design of an imaging heavy ion beam probe for ASDEX Upgrade," J. Instrum. **14**, C10030 (2019).

[20] G. Birkenmeier, J. Galdon-Quiroga, V. Olevskaia, P. Oyola, J. J. Toledo-Garrido, K. Bald, M. Sochor, G. Anda, S. Zoletnik, A. Herrmann, V. Rohde, M. Teschke, L. Giannone, T. Lunt, E. Viezzer, M. Garcia-Munoz, and ASDEX Upgrade Team, "Hardware developments and commissioning of the imaging heavy ion beam probe at ASDEX upgrade," Fusion Eng. Des. **168**, 112644 (2021).

[21] K. Kadota, K. Tsuchida, Y. Kawasumi, and J. Fujita, "Plasma diagnostics by neutral beam probing," Plasma Phys. **20**, 1011 (1978).

[22] E. Wolfrum, F. Aumayr, D. Wutte, H. Winter, E. Hintz, D. Rusbüldt, and R. P. Schorn, "Fast lithium-beam spectroscopy of tokamak edge plasmas," Rev. Sci. Instrum. **64**, 2285–2292 (1993).

[23] D. M. Thomas, "Poloidal magnetic field measurements and analysis with the DIII-D LIBEAM system (invited)," Rev. Sci. Instrum. **74**, 1541–1546 (2003).

[24] D. M. Thomas, G. R. McKee, K. H. Burrell, F. Levinton, E. L. Foley, and R. K. Fisher, "Chapter 6: Active spectroscopy," Fusion Sci. Technol. **53**, 487–527 (2008).

[25] M. Berta, G. Anda, M. Aradi, A. Bencze, C. Buday, I. G. Kiss, S. Tulipán, G. Veres, S. Zoletnik, J. Havlícek, and P. Háček, "Development of atomic beam probe for tokamaks," Fusion Eng. Des. **88**, 2875–2880 (2013).

[26] S. Zoletnik, G. Anda, M. Aradi, O. Asztalos, S. Bató, A. Bencze, M. Berta, G. Demeter, D. Dunai, P. Hacek, S. Hegedűs, G. H. Hu, T. Krizsanóczi, M. Lampert,

03 November 2026 15:33:44

© Author(s) 2024

D. Nagy, J. Németh, M. Otte, G. Petravich, G. I. Pokol, D. Réfy, B. Tál, and M. Vécsei, "Advanced neutral alkali beam diagnostics for applications in fusion research (invited)," Rev. Sci. Instrum. **89**, 10–107 (2018).
[27]K. Ishii, M. Kotoku, T. Segawa, I. Katanuma, A. Mase, and S. Miyoshi, "Thermal barrier potential and two-dimensional space-potential measurements with gold neutral-beam probes in GAMMA 10," Rev. Sci. Instrum. **60**, 3270–3274 (1989).
[28]E. Saravia, J. Castracane, and J. T. Woo, "Neutral beam probe for edge plasma analysis in tokamaks," Rev. Sci. Instrum. **61**, 3528–3531 (1990).
[29]H. Iguchi, K. Takasugi, T. Shoji, J. F. Junji Fujita, and H. I. Hideo Ikegami, "Simultaneous measurements of plasma potential and density fluctuations in a bumpy torus by a heavy neutral beam probe," Jpn. J. Appl. Phys. **32**, 1829 (1993).
[30]M. Mizuguchi, M. Yoshikawa, Y. Miyata, S. Goshu, M. Nakada, Y. Oono, Y. Nakashima, and T. Imai, "Study of radial potential fluctuations by using a gold neutral beam probe system," Rev. Sci. Instrum. **79**, 10F309 (2008).
[31]P. Hacek, M. Berta, G. Anda, M. Aradi, A. Bencze, D. Dunai, J. Krbec, R. Panek, D. I. Refy, J. Stockel, V. Weinzettl, and S. Zoletnik, "Development of an ion beam detector for the atomic beam probe diagnostic," Rev. Sci. Instrum. **89**, 113506 (2018).
[32]D. I. Réfy, S. Zoletnik, D. Dunai, G. Anda, M. Lampert, S. Hegedűs, D. Nagy, M. Palánkai, J. Kádi, B. Leskó, M. Aradi, P. Hacek, and V. Weinzettl, "Micro-Faraday cup matrix detector for ion beam measurements in fusion plasmas," Rev. Sci. Instrum. **90**, 033501 (2019).
[33]G. Anda, D. Dunai, M. Lampert, T. Krizsanóczi, J. Németh, S. Bató, Y. U. Nam, G. H. Hu, and S. Zoletnik, "Development of a high current 60 keV neutral lithium beam injector for beam emission spectroscopy measurements on fusion experiments," Rev. Sci. Instrum. **89**, 013503 (2018).
[34]J. J. Toledo-Garrido, J. Galdon-Quiroga, E. Viezzer, G. Birkenmeier, V. Olevskaia, M. Balden, J. Garcia-Lopez, M. C. Jimenez-Ramos, M. Rodriguez-Ramos, G. Anda, M. Videla-Trevin, and M. Garcia-Munoz, "Characterization of scintillator screens under irradiation of low energy ^{133}Cs ions," J. Instrum. **17**, P02026 (2022).
[35]M. Rodríguez-Ramos, M. C. Jiménez-Ramos, M. García-Muñoz, and J. García López, "Temperature response of several scintillator materials to light ions," Nucl. Instrum. Methods Phys. Res., Sect. B **403**, 7–12 (2017).
[36]D. Cruz-Zabala, "Characterization of the ion pedestal in low and high collisionality plasmas," M.S. Thesis, University of Seville (2017).
[37]P. Oyola, J. Gonzalez-Martin, M. Garcia-Munoz, J. Galdon-Quiroga, G. Birkenmeier, E. Viezzer, J. Dominguez-Palacios, J. Rueda-Rueda, J. F. Rivero-Rodriguez, and Y. Todo, "Implementation of synthetic fast-ion loss detector and imaging heavy ion beam probe diagnostics in the 3D hybrid kinetic-MHD code MEGA," Rev. Sci. Instrum. **92**, 043558 (2021).
[38]P. A. Schneider, "Characterization and scaling of the tokamak edge transport barrier," Ph.D. Thesis, Ludwig Maximilian University (2012).
[39]A. Jansen van Vuuren, B. Geiger, P. Schneider, K. Bogar, P. Poloskei, A. Cathey, M. Hoelzl, A. Jacobsen, M. Cavedon, R. Dux, and ASDEX Upgrade Team, "Experimental study of ELM induced fast-ion transport using passive FIDA spectroscopy at the ASDEX Upgrade tokamak," Nucl. Fusion **61**, 046001 (2021).
[40]T. Ido, Y. Miura, K. Kamiya, Y. Hamada, K. Hoshino, A. Fujisawa, K. Itoh, S.-I. Itoh, A. Nishizawa, H. Ogawa, Y. Kusama, and JFT-2M Group, "Geodesic–acoustic-mode in JFT-2M tokamak plasmas," Plasma Phys. Controlled Fusion **48**, S41 (2006).
[41]A. Ashourvan, R. Nazikian, E. Belli, J. Candy, D. Eldon, B. A. Grierson, W. Guttenfelder, S. R. Haskey, C. Lasnier, G. R. McKee, and C. C. Petty, "Formation of a high pressure staircase pedestal with suppressed edge localized modes in the DIII-D tokamak," Phys. Rev. Lett. **123**, 115001 (2019).
[42]F. M. Laggner, E. Wolfrum, M. Cavedon, F. Mink, E. Viezzer, M. G. Dunne, P. Manz, H. Doerk, G. Birkenmeier, R. Fischer, S. Fietz, M. Maraschek, M. Willensdorfer, and F. Aumayr, "High frequency magnetic fluctuations correlated with the inter-ELM pedestal evolution in ASDEX Upgrade," Plasma Phys. Controlled Fusion **58**, 065005 (2016).
[43]G. Birkenmeier, F. M. Laggner, M. Willensdorfer, T. Kobayashi, P. Manz, E. Wolfrum, D. Carralero, R. Fischer, B. Sieglin, G. Fuchert, and U. Stroth, "Magnetic field dependence of the blob dynamics in the edge of ASDEX upgrade L-mode plasmas," Plasma Phys. Controlled Fusion **56**, 075019 (2014).
[44]D. A. D'Ippolito, J. R. Myra, and S. J. Zweben, "Convective transport by intermittent blob-filaments: Comparison of theory and experiment," Phys. Plasmas **18**, 060501 (2011).
[45]G. Birkenmeier, P. Manz, D. Carralero, F. M. Laggner, G. Fuchert, K. Krieger, H. Maier, F. Reimold, K. Schmid, R. Dux, T. Pütterich, M. Willensdorfer, and E. Wolfrum, "Filament transport, warm ions and erosion in ASDEX Upgrade L-modes," Nucl. Fusion **55**, 033018 (2015).
[46]C. P. Chrobak, M. A. Van Zeeland, R. A. Moyer, and J. H. Yu, "Restoring transmission of irradiated image fiber bundles," Rev. Sci. Instrum. **83**, 10E514 (2012).

03 November 2026 15:33:44

© Author(s) 2024